Supplemental Material for Spectral and thermodynamic properties of the Holstein polaron: Hierarchical equations of motion approach

Veljko Janković[1,*] and Nenad Vukmirović[1,†]

[1] *Institute of Physics Belgrade, University of Belgrade, Pregrevica 118, 11080 Belgrade, Serbia*

I. GREEN'S FUNCTIONS AND SPECTRAL FUNCTION

The fluctuation–dissipation theorem for single-particle Green's functions states that the spectral function, which is defined as

$$A(k,\omega) = -\frac{1}{\pi}\mathrm{Im}\, G^R(k,\omega), \tag{1}$$

is related to the greater and lesser Green's functions as follows[1]

$$A(k,\omega) = -\frac{1}{2\pi}\mathrm{Im}\, G^{>}(k,\omega)\left(1+e^{-\beta\hbar\omega}\right), \tag{2}$$

$$A(k,\omega) = \frac{1}{2\pi}\mathrm{Im}\, G^{<}(k,\omega)\left(1+e^{\beta\hbar\omega}\right). \tag{3}$$

The Lehmann representation of $G^{>}(k,\omega)$ reads as

$$G^{>}(k,\omega) = -\frac{2\pi i}{Z}\sum_{nm} e^{-\beta E_n}\,\delta(\omega+\omega_n-\omega_m)\left|\langle n\left|c_k\right|m\rangle\right|^2, \tag{4}$$

where state $|m\rangle$ belongs to the single-excitation subspace, while state $|n\rangle$ belongs to the zero-excitation subspace. It is thus advantageous to separate out the vertical excitation energy ε_e from ω_n by $\omega_n = \varepsilon_e/\hbar + \Delta\omega_n$ and to shift the zero of the frequency axis to $\varepsilon_e/\hbar$ by defining $G^{>}_{\mathrm{shifted}}(k,\omega) = G^{>}(\omega+\varepsilon_e/\hbar)$. The corresponding spectral function $A_{\mathrm{shifted}}(k,\omega) = A(k,\omega+\varepsilon_e/\hbar)$ then reads as

$$A_{\mathrm{shifted}}(k,\omega) = -\frac{1}{2\pi}\mathrm{Im}\, G^{>}_{\mathrm{shifted}}(k,\omega)\left(1+e^{-\beta\hbar\omega}e^{-\beta\varepsilon_e}\right) \approx -\frac{1}{2\pi}\mathrm{Im}\, G^{>}_{\mathrm{shifted}}(k,\omega) \tag{5}$$

under the physically plausible assumption that $\beta\varepsilon_e \gg 1$.

Using similar ideas, the Lehmann representation of $G^{<}(k,\omega)$ is transformed as follows

$$G^{<}(k,\omega) = \frac{2\pi i}{Z}\,e^{-\beta\varepsilon_e}\sum_{nm} e^{-\beta\hbar\Delta\omega_m}\,\delta(\omega-\varepsilon_e/\hbar+\omega_n-\Delta\omega_m)\left|\langle n\left|c_k\right|m\rangle\right|^2. \tag{6}$$

Defining

$$G^{<}_{\mathrm{shifted}}(k,\omega) = e^{\beta\varepsilon_e}\,G^{<}(k,\omega+\varepsilon_e/\hbar), \tag{7}$$

and employing $\beta\varepsilon_e \gg 1$, we finally obtain that

$$A_{\mathrm{shifted}}(k,\omega) = \frac{1}{2\pi}\mathrm{Im}\, G^{<}_{\mathrm{shifted}}(k,\omega)\cdot e^{\beta\hbar\omega}. \tag{8}$$

In the main body of the manuscript, we will not insist on notation $G^{>/<}_{\mathrm{shifted}}(k,\omega), A_{\mathrm{shifted}}(k,\omega)$, which simply shifts the origin of the energy scale from the energy of the unexcited state to the vertical excitation energy of the singly-excited state. The latter choice is far more common in the literature.

II. QMC METHOD FOR THERMODYNAMIC EXPECTATION VALUES

A. Operators that depend on electronic coordinates only

We now describe the calculation of the expectation value of the operators that depend on electronic coordinates only, such as the free electronic operator $H_{\rm e}$ and the operator $n_k = |k\rangle\langle k|$ of the number of electrons of momentum k. The expectation value of such an operator O is given as

$$\langle O\rangle = \frac{\sum_{ab}\int \mathrm{d}\{x\}\ \langle a\{x\}|e^{-\beta H}|b\{x\}\rangle\ \langle b|O|a\rangle}{\sum_{ab}\int \mathrm{d}\{x\}\ \langle a\{x\}|e^{-\beta H}|b\{x\}\rangle\,\delta_{ab}} \tag{9}$$

To evaluate the integrals, we express $\langle a\{x\}|e^{-\beta H}|b\{x\}\rangle$ using Eq. (63) in the main part of the paper and we analytically calculate the Gaussian integrals over the phononic coordinates using Eq. (68) in the main part of the paper.

Equation (9) then takes the form

$$\langle O\rangle = \frac{\mathcal{N}_1}{\mathcal{D}_1} \tag{10}$$

with

$$\mathcal{N}_1 = \sum_{ab}\sum_{j_1\ldots j_{K-1}} f(j_1)f(j_2)\ldots f(j_{K-1})f\left(a-b-\sum_{i=1}^{K-1} j_i\right)e^{\frac{1}{2}\mathbf{b}\cdot\mathbf{A}^{-1}\cdot\mathbf{b}}\,\langle b|O|a\rangle \tag{11}$$

and

$$\mathcal{D}_1 = \sum_{ab}\sum_{j_1\ldots j_{K-1}} f(j_1)f(j_2)\ldots f(j_{K-1})f\left(a-b-\sum_{i=1}^{K-1} j_i\right)e^{\frac{1}{2}\mathbf{b}\cdot\mathbf{A}^{-1}\cdot\mathbf{b}}\delta_{ab}. \tag{12}$$

We then perform Monte Carlo summation in the same way as for the correlation function.

The results presented in Fig. 2(a) and 2(c) of the paper were obtained with 10^7 samples and $K = 80$.

The results presented in Figs. 5 and 6 in this Supplemental Material were obtained with 10^5 samples and $K = 80$, except for Fig. 6(b) where $K = 200$.

B. Interaction energy and fermion-boson correlation function

Next, we describe Monte Carlo calculation of averages of the operator of electron-phonon interaction $H_{\rm e-ph}$ and the fermion-boson correlation function $\mathcal{C}(l) = \sum_i |i\rangle\langle i|\left(b^\dagger_{i+l} + b_{i+l}\right)$. Expectation values of these operators read

$$\langle H_{\rm e-ph}\rangle = \frac{\sum_a\int \mathrm{d}\{x\}\ \langle a\{x\}|e^{-\beta H}|a\{x\}\rangle\, x_a\gamma\sqrt{\frac{2m\omega_0}{\hbar}}}{\sum_a\int \mathrm{d}\{x\}\ \langle a\{x\}|e^{-\beta H}|a\{x\}\rangle} \tag{13}$$

and

$$\langle \mathcal{C}(l)\rangle = \frac{\sum_a\int \mathrm{d}\{x\}\ \langle a\{x\}|e^{-\beta H}|a\{x\}\rangle\, x_{a+l}\sqrt{\frac{2m\omega_0}{\hbar}}}{\sum_a\int \mathrm{d}\{x\}\ \langle a\{x\}|e^{-\beta H}|a\{x\}\rangle}. \tag{14}$$

To evaluate the integrals in the numerator, we exploit the identity

$$\int \mathrm{d}^n\mathbf{z}\, z_a e^{-\frac{1}{2}\mathbf{z}\cdot\mathbf{A}\cdot\mathbf{z}}e^{\mathbf{b}\cdot\mathbf{z}} = (2\pi)^{n/2}(\det\mathbf{A})^{-1/2}e^{\frac{1}{2}\mathbf{b}\cdot\mathbf{A}^{-1}\cdot\mathbf{b}}\left(\mathbf{A}^{-1}\cdot\mathbf{b}\right)_a \tag{15}$$

and obtain

$$\langle H_{\rm e-ph}\rangle = \frac{\mathcal{N}_2}{\mathcal{D}_2} \tag{16}$$

with

$$\mathcal{N}_2 = \sum_a \sum_{j_1 \ldots j_{K-1}} f(j_1) f(j_2) \ldots f(j_{K-1}) f\left(-\sum_{i=1}^{K-1} j_i\right) e^{\frac{1}{2}\mathbf{b}\cdot\mathbf{A}^{-1}\mathbf{b}} \left(\mathbf{A}^{-1}\mathbf{b}\right)_a \gamma \sqrt{\frac{2m\omega_0}{\hbar}} \tag{17}$$

and

$$\mathcal{D}_2 = \sum_a \sum_{j_1 \ldots j_{K-1}} f(j_1) f(j_2) \ldots f(j_{K-1}) f\left(-\sum_{i=1}^{K=1} j_i\right) e^{\frac{1}{2}\mathbf{b}\cdot\mathbf{A}^{-1}\cdot\mathbf{b}}. \tag{18}$$

We find as well

$$\langle \mathcal{C}(l) \rangle = \frac{\mathcal{N}_3}{\mathcal{D}_2} \tag{19}$$

with

$$\mathcal{N}_3 = \sum_a \sum_{j_1 \ldots j_{K-1}} f(j_1) f(j_2) \ldots f(j_{K-1}) f\left(-\sum_{i=1}^{K-1} j_i\right) e^{\frac{1}{2}\mathbf{b}\cdot\mathbf{A}^{-1}\mathbf{b}} \left(\mathbf{A}^{-1}\mathbf{b}\right)_{a+l} \sqrt{\frac{2m\omega_0}{\hbar}}. \tag{20}$$

The sums are then evaluated using the Monte Carlo method in the same way as in previous cases.

The results presented in Fig. 2(b) of the paper were obtained with 10^6 samples and $K = 80$, while the results in Fig. 2(d) of the paper were obtained with 10^7 samples and $K = 80$.

III. WEAK-COUPLING LIMIT: RAYLEIGH–SCHRÖDINGER PERTURBATION THEORY

Truncating the HEOM [Eq. (30) of the main text] at depth 1, we remain with the following equations

$$\partial_t G^{>}(k,t) = -i\Omega_k G^{>}(k,t) + i\sum_{qm} G^{(>,1)}_{\mathbf{0}^+_{qm}}(k-q,t), \tag{21}$$

$$\partial_t G^{(>,1)}_{\mathbf{0}^+_{qm}}(k-q,t) = -i\left[\Omega_{k-q} + \omega_q(\delta_{m0}-\delta_{m1})\right] G^{(>,1)}_{\mathbf{0}^+_{qm}}(k-q,t) + i\omega_0^2 c_{qm} G^{>}(k,t). \tag{22}$$

Separating out the free-rotation contribution from $G^{>}$ by defining $G^{>}(k,t) = e^{-i\Omega_k t}\mathcal{G}^{>}(k,t)$, the integration of Eq. (22) leads to

$$G^{(>,1)}_{\mathbf{0}^+_{qm}}(k-q,t) = i\omega_0^2 c_{qm}\int_0^t ds\, \exp\left\{i\left[\Omega_k - \Omega_{k-q} - \omega_q(\delta_{m0}-\delta_{m1})\right]s\right\} e^{-i\Omega_k t}\mathcal{G}^{>}(k,t-s). \tag{23}$$

The Markov approximation $\mathcal{G}^{>}(k,t-s) \approx \mathcal{G}^{>}(t)$ assumes that $\mathcal{G}^{>}$ changes very slowly in time, so that its value at time $t-s$ is approximately equal to its value at time t. The remaining integration can be performed analytically. Nevertheless, one may resort to the so-called adiabatic approximation, in which the upper limit of the integral t is replaced by $+\infty$. Physically, this means that the last scattering on phonons that is relevant to the properties at time t happened in the distant past. Moreover, to ensure the integral convergence, one adds a small and positive imaginary part to the frequency difference. Finally,

$$\begin{aligned} G^{(>,1)}_{\mathbf{0}^+_{qm}}(k-q,t) &\approx G^{>}(k,t)\times i\omega_0^2 c_{qm}\int_0^{+\infty} ds\, \exp\left\{i\left[\Omega_k - \Omega_{k-q} - \omega_q(\delta_{m0}-\delta_{m1}) + i\eta\right]s\right\} \\ &= \frac{-\omega_0^2 c_{qm}}{\Omega_k - \Omega_{k-q} - \omega_q(\delta_{m0}-\delta_{m1}) + i\eta} G^{>}(k,t). \end{aligned} \tag{24}$$

We now insert Eq. (24) into Eq. (21) and transfer to the frequency domain. Keeping in mind that Eq. (21) is solved for $t > 0$ under the initial condition $G^{>}(k,t=0) = -i$, we finally obtain

$$G^{>}(k,\omega) = \frac{1}{\omega - \Omega_k - \Sigma_k} \tag{25}$$

where the one-phonon self-energy reads as

$$\Sigma_k = \sum_{qm} \frac{\omega_0^2 c_{qm}}{\Omega_k - \Omega_{k-q} - \omega_q(\delta_{m0}-\delta_{m1}) + i\eta}. \tag{26}$$

The real part of the self-energy brings about the energy renormalization

$$\mathrm{Re}\,\Sigma_k = \frac{\gamma^2}{\hbar}\frac{1}{N}\sum_q \left(\frac{1+n_{\mathrm{BE}}(\omega_q,T)}{\hbar\Omega_k - \hbar\Omega_{k-q} - \hbar\omega_q} + \frac{n_{\mathrm{BE}}(\omega_q,T)}{\hbar\Omega_k - \hbar\Omega_{k-q} + \hbar\omega_q}\right) \tag{27}$$

while its imaginary part

$$\mathrm{Im}\,\Sigma_k = -\pi\frac{\gamma^2}{\hbar}\frac{1}{N}\sum_q \left\{[1+n_{\mathrm{BE}}(\omega_q,T)]\delta(\hbar\Omega_k - \hbar\Omega_{k-q} - \hbar\omega_q) + n_{\mathrm{BE}}(\omega_q,T)\delta(\hbar\Omega_k - \hbar\Omega_{k-q} + \hbar\omega_q)\right\} \tag{28}$$

is related to the second-order result for carrier scattering time τ_k via $\tau_k^{-1} = -2\mathrm{Im}\,\Sigma_k$.

IV. SINGLE-SITE LIMIT: LANG–FIRSOV RESULTS

Here, we explicitly present the steps that are needed to reduce the exact Feynman–Vernon results presented in the main text to the Lang–Firsov results in the limit of vanishing electronic coupling. While these results are by no means new (see, e.g., Ch. 4 of Ref. 1), we feel that it is important to demonstrate how our approach reduces to this important limiting case.

We start from the computation of $G^{>}$. The exact solution in the single-site limit reduces to

$$G^{>}(t) = -ie^{-i\varepsilon_e t/\hbar} \exp\left[-\omega_0^2 \int_0^t ds_2 \int_0^{s_2} ds_1 \sum_m c_m e^{-\mu_m(s_2-s_1)}\right]. \tag{29}$$

To obtain this result, we used the fact that, in the single-site limit, the operator V_q reduces to $|j\rangle\langle j|$, which is time-independent, so that the time-ordering sign entering the exact solution is not effective. Solving the integral under the exponential we finally obtain

$$G^{>}(t) = -ie^{-i\varepsilon_e t/\hbar}\, e^{-(\gamma/(\hbar\omega_0))^2(2N_{\rm ph}+1)} \exp\left[\left(\frac{\gamma}{\hbar\omega_0}\right)^2 \left((1+N_{\rm ph})e^{-i\omega_0 t} + N_{\rm ph}e^{i\omega_0 t} + i\omega_0 t\right)\right], \tag{30}$$

where $N_{\rm ph} = \left(e^{\beta\hbar\omega_0}-1\right)^{-1}$. The exact result for $G^{>}(\omega)$ can then be obtained following the procedure from Ref. 1 The crux of the derivation is to employ the following identity[2]

$$e^{z\cos\theta} = \sum_{l=-\infty}^{+\infty} I_l(z)\, e^{il\theta}, \tag{31}$$

where $I_l(z)$ are the Bessel functions of complex argument.

A similar procedure can be repeated to obtain the single-site limit of the exact result for $G^{<}$:

$$G^{<}(t) = ie^{-i\varepsilon_e t/\hbar} e^{-\beta[\varepsilon_e - \gamma^2/(\hbar\omega_0)]}\, e^{-(\gamma/(\hbar\omega_0))^2(2N_{\rm ph}+1)} \exp\left[\left(\frac{\gamma}{\hbar\omega_0}\right)^2 \left((1+N_{\rm ph})e^{i\omega_0 t} + N_{\rm ph}e^{-i\omega_0 t} + i\omega_0 t\right)\right]. \tag{32}$$

Apart from the prefactors, the only difference between the single-site expressions for $G^{>}$ and $G^{<}$ is the place of phonon factors $1+N_{\rm ph}\pm 1$ in front of exponentials $e^{\pm i\omega_0 t}$.

While $G^{>/<}(\omega)$ is an infinite series of equidistant δ peaks of varying intensity, one commonly introduces the artificial broadening η, i.e., replaces δ peaks by Lorentzians whose full width at half maximum is equal to η. To take the artificial broadening into account, it is enough to replace

$$\mu_0 = i\omega_0 \to i\omega_0 + \eta, \quad \mu_1 = -i\omega_0 \to -i\omega_0 + \eta. \tag{33}$$

Equation (30) then becomes

$$\begin{aligned} G^{>}(t) = &-ie^{-i\varepsilon_e t/\hbar}\, e^{-(\gamma/(\hbar\omega_0))^2(2N_{\rm ph}+1)} \\ &\times \exp\left[\left(\frac{\gamma}{\hbar\omega_0}\right)^2 \left((1+N_{\rm ph})e^{-i(\omega_0 - i\eta)t} + N_{\rm ph}e^{i(\omega_0+i\eta)t} + i(\omega_0 + i(2N_{\rm ph}+1)\eta)t\right)\right], \end{aligned} \tag{34}$$

while Eq. (32) becomes

$$\begin{aligned} G^{<}(t) = &ie^{-i\varepsilon_e t/\hbar} e^{-\beta[\varepsilon_e - \gamma^2/(\hbar\omega_0)]}\, e^{-(\gamma/(\hbar\omega_0))^2(2N_{\rm ph}+1)} \\ &\times \exp\left[\left(\frac{\gamma}{\hbar\omega_0}\right)^2 \left((1+N_{\rm ph})e^{i(\omega_0 + i\eta)t} + N_{\rm ph}e^{-i(\omega_0-i\eta)t} + i(\omega_0 + i(2N_{\rm ph}+1)\eta)t\right)\right]. \end{aligned} \tag{35}$$

On the other hand, the replacements of Eq. (33) affect the hierarchy through its kinetic term only, while the hierarchical links remain unaffected. In more detail,

$$\begin{aligned} \left[\partial_t G^{(n)}_{\mathbf{n}}(k-k_{\mathbf{n}},t)\right]_{\rm kin} &= -i(\omega_{k-k_{\mathbf{n}}} + \mu_{\mathbf{n}})G^{(n)}_{\mathbf{n}}(k-k_{\mathbf{n}},t) \\ &\to -i(\omega_{k-k_{\mathbf{n}}} + \mu_{\mathbf{n}} - in\eta)G^{(n)}_{\mathbf{n}}(k-k_{\mathbf{n}},t), \end{aligned} \tag{36}$$

so that the auxiliary Green's functions at depth n are damped at rate $n\eta$. Analytical and numerical result exhibit excellent agreement in the single-site limit, which is demonstrated in Fig. 1 for $\gamma/\omega_0 = \sqrt{2}$ and $k_BT/\omega_0 = 1$ and different values of the artificial broadening $\eta/\omega_0 = 0, 0.01, 0.02$.

The influence of η on the spectral properties in the single-site limit are summarized in Fig. 2.

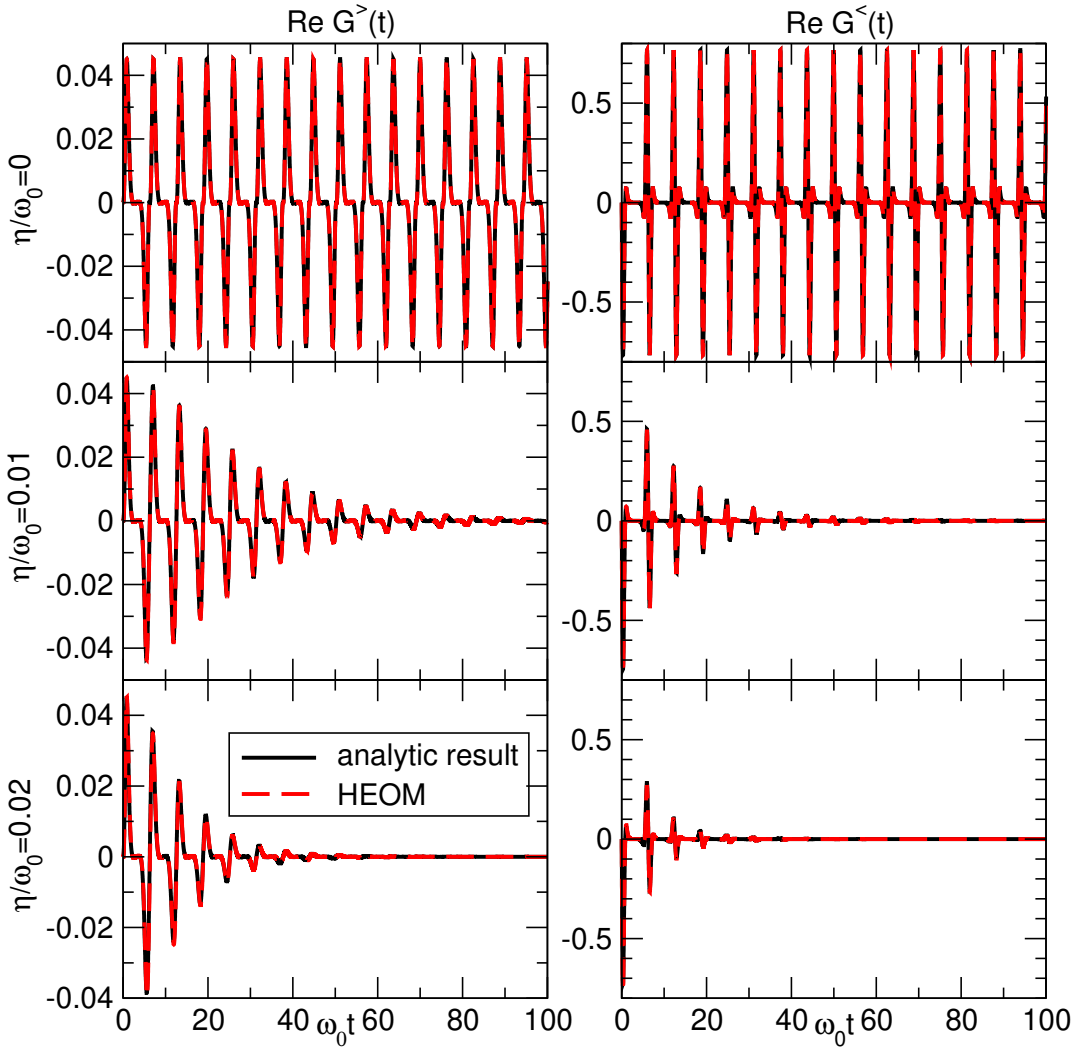

Figure 1. Results for $G^{>}(t)$ (left panels) and $G^{<}(t)$ (right panels) in the single-site limit for $\gamma/\omega_0 = \sqrt{2}$, $k_BT/\omega_0 = 1$ and different values of the artificial broadening $\eta = 0$ (upper panels), $\eta/\omega_0 = 0.01$ (middle panels), and $\eta/\omega_0 = 0.02$ (bottom panels). Without loss of generality, we assume that $\varepsilon_e = 0$. Analytical results are obtained using Eqs. (34) and (35), while the kinetic terms in the HEOM assume the form of Eq. (36).

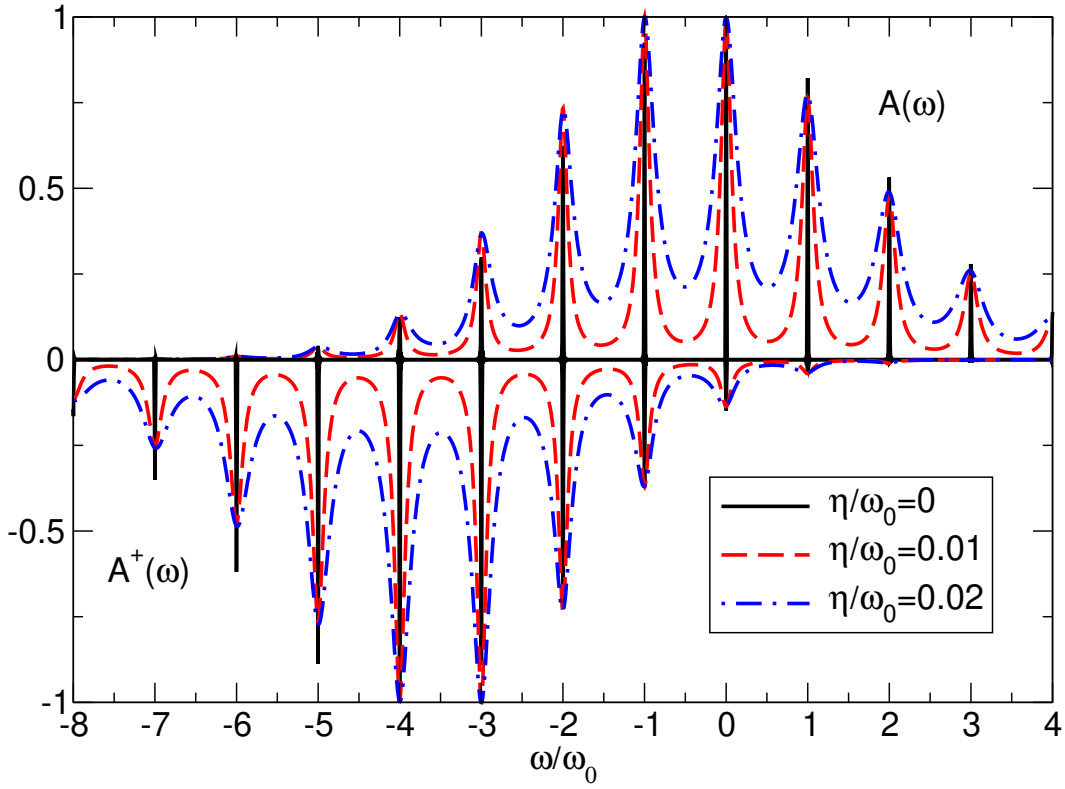

Figure 2. Electron-addition $[A(\omega) = -\frac{1}{2\pi}\mathrm{Im}\, G^{>}(\omega)]$ and electron-removal $[A^{+}(\omega) = \frac{1}{2\pi}\mathrm{Im}\, G^{<}(\omega)]$ spectral functions for a single site with $\gamma/\omega_0 = \sqrt{2}$ and $k_B T/\omega_0 = 1$ and different levels of the artificial broadening $\eta/\omega_0 = 0, 0.01, 0.02$. Both $A(\omega)$ and $A^{+}(\omega)$ are normalized so that their maximum values are equal to 1. $A(\omega)$ is presented in the positive half-plane, while $A^{+}(\omega)$ is presented in the negative half-plane. This style of presentation emphasises the fact that $A(\omega)$ and $A^{+}(\omega)$ are mirror images of one another around $\omega_{\mathrm{QP}}/\omega_0 = -(\gamma/\omega_0)^2 = -2$.

V. ARTIFICIAL BROADENING OF SPECTRAL LINES

When the spectral density of the electron–phonon coupling is that of an underdamped Brownian oscillator

$$\mathcal{J}(\omega) = \Lambda \left[\frac{\omega\eta}{(\omega-\omega_0)^2+\eta^2} + \frac{\omega\eta}{(\omega+\omega_0)^2+\eta^2} \right] \tag{37}$$

the bath correlation function assumes the following form[3]

$$\mathcal{C}_{q_2q_1}(t) = \delta_{q_2,-q_1} (\hbar\omega_0)^2 \sum_{m=0}^{+\infty} c_m \, e^{-\mu_m t} \tag{38}$$

where

$$c_0 = \frac{\Lambda}{\hbar\omega_0} \left(1 - i\frac{\eta}{\omega_0} \right) \left[1 + n_{\mathrm{BE}}(\hbar\omega_0 - i\hbar\eta, T) \right], \quad \mu_0 = i\omega_0 + \eta \tag{39}$$

$$c_1 = \frac{\Lambda}{\hbar\omega_0} \left(1 + i\frac{\eta}{\omega_0} \right) n_{\mathrm{BE}}(\hbar\omega_0 + i\hbar\eta, T), \quad \mu_1 = -i\omega_0 + \eta \tag{40}$$

$$c_m = -4\frac{\eta}{\omega_0} \frac{\Lambda k_B T}{(\hbar\omega_0)^2} \rho_{m-1} \frac{\xi_{m-1}}{\beta\hbar\omega_0} \frac{1 - \left(\frac{\xi_{m-1}}{\beta\hbar\omega_0}\right)^2 + \left(\frac{\eta}{\omega_0}\right)^2}{\left[1 - \left(\frac{\xi_{m-1}}{\beta\hbar\omega_0}\right)^2 + \left(\frac{\eta}{\omega_0}\right)^2 \right]^2 + 4\frac{\xi_{m-1}}{\beta\hbar\omega_0}}, \quad \mu_m = \frac{\xi_{m-1}}{\beta\hbar}, \quad m \geq 2 \tag{41}$$

In Eq. (41), ξ_m and ρ_m (for $m \geq 1$) are the poles and residues of the Bose–Einstein function $(e^z - 1)^{-1}$ in the upper half of the complex plane. The corresponding decomposition of the Bose–Einstein function into simple poles reads as

$$\frac{1}{e^z - 1} = -\frac{1}{2} + \frac{1}{z} + \sum_{m=1}^{+\infty} \rho_m \left(\frac{1}{z - i\xi_m} + \frac{1}{z + i\xi_m} \right). \tag{42}$$

In the Matsubara decomposition, $\xi_m = 2\pi m$, $\rho_m = 1$. There are other possible choices, e.g., Padé decomposition.

Let us now assume that $\hbar\eta$ is the smallest energy scale in the problem, i.e., $\hbar\eta \ll k_B T$ and $\eta \ll \omega_0$. One may then neglect the imaginary parts of c_0 and c_1. For $m \geq 2$, c_m is linear in the small quantity η/ω_0, while the corresponding exponential factor $e^{-\mu_m t}$ decays much faster than $e^{-\mu_{0/1} t}$ because of $\xi_{m-1}/(\beta\hbar\eta) \gg 1$. We may thus completely discard the infinite-series part of the bath correlation function, after which it reduces to

$$\mathcal{C}_{q_2q_1}(t) = \delta_{q_2,-q_1} \frac{\Lambda}{\hbar\omega_0} \left\{ [1 + n_{\mathrm{BE}}(\omega_0, T)] e^{-(i\omega_0+\eta)t} + n_{\mathrm{BE}}(\omega_0, T) e^{-(-i\omega_0+\eta)t} \right\}. \tag{43}$$

By identifying $\Lambda = \gamma^2/(\hbar\omega_0)$, we obtain the expression that is identical to the bath correlation function presented in the main text, with the only difference that the oscillatory terms are replaced by damped oscillatory terms.

VI. COMPARISON BETWEEN TIME-DOMAIN AND FREQUENCY-DOMAIN HEOM DATA FOR DIFFERENT MAXIMUM HIERARCHY DEPTHS

In Figs. 3 and 4, we compare the real part of the envelope $\mathcal{G}^{>}(k,t)$ of the greater Green's function and the spectral function $A(k,\omega)$ for three different values of the maximum hierarchy depth D in the following regime of model parameters: $k_BT/J = 0.4$, $\hbar\omega_0/J = 1$, $\gamma/J = \sqrt{2}$, $N = 8$.

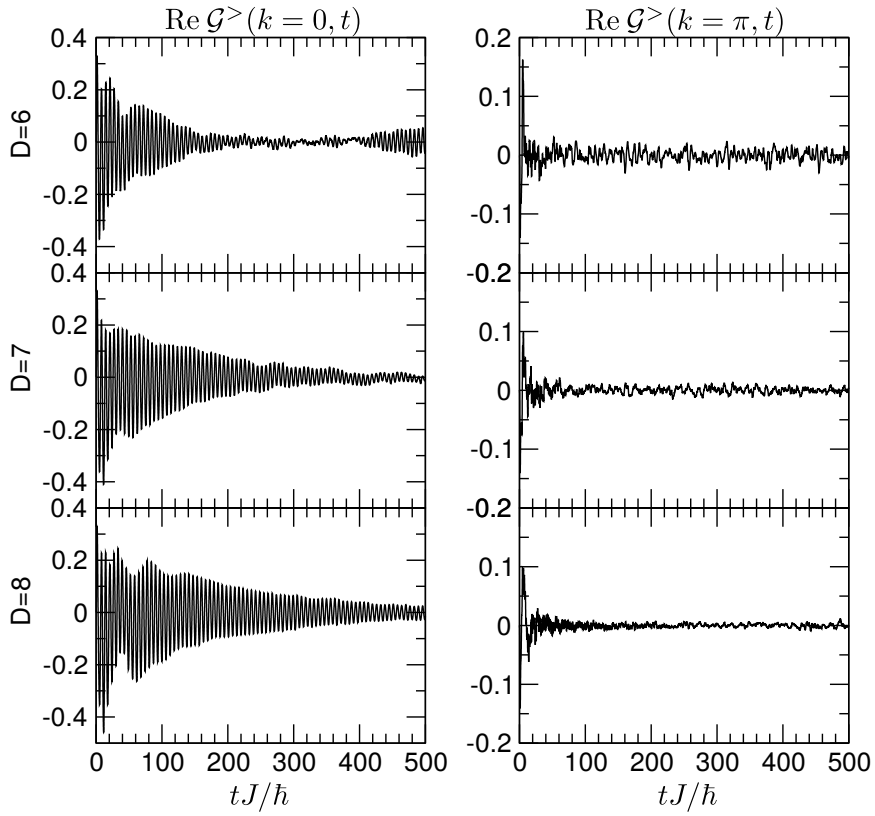

Figure 3. Time dependence of the real part of the envelope of the greater Green's function, Re $\mathcal{G}^{>}(k,t)$, for three different values of the maximum hierarchy depth ($D = 6$ in the upper panels, $D = 7$ in the middle panels, and $D = 8$ in the lower panels) and for two different values of the dimensionless wave number ($k = 0$ in the left column, $k = \pi$ in the right column). The ranges on the vertical axes on all three left-column plots are the same ($[-0.5, 0.4]$), as are their counterparts on all three right-column plots ($[-0.2, 0.2]$).

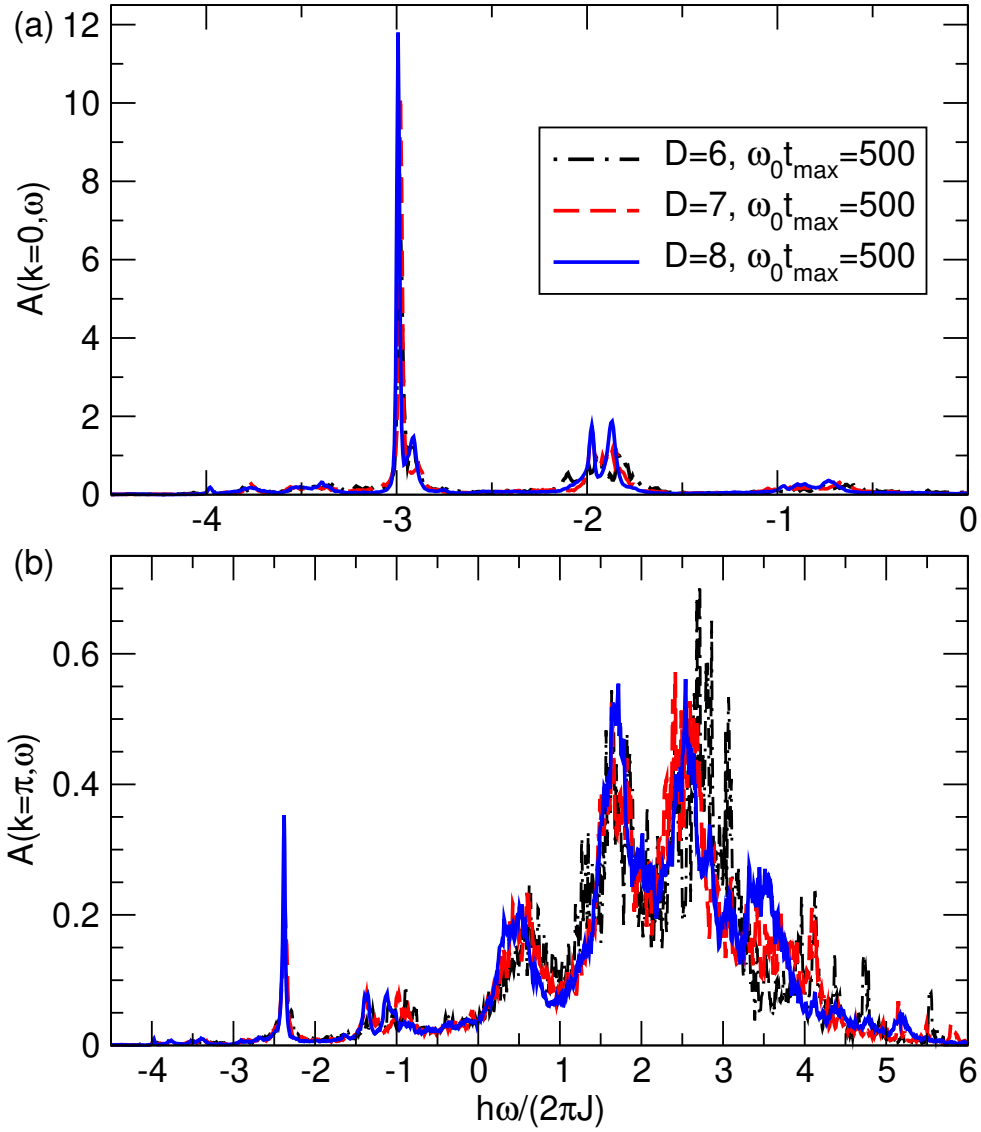

Figure 4. Spectral function $A(k,\omega)$ for three different values of the maximum hierarchy depth ($D = 6$ is represented by dash-dotted black lines, $D = 7$ is represented by dashed red lines, $D = 8$ is represented by solid blue lines) and for two different values of the dimensionless wave number ($k = 0$ in the upper panel and $k = \pi$ in the lower panel). All the time-domain data presented in Fig. 3 are used to compute $A(k,\omega)$, which is signalized by the label $\omega_0 t_{\max} = 500$ in the legend.

VII. COMPARISON BETWEEN QMC AND HEOM RESULTS FOR THE ELECTRONIC MOMENTUM DISTRIBUTION

In Fig. 5 we compare QMC and HEOM predictions for the electronic momentum distribution for two different temperatures, $k_BT/J = 1$ in Figs. 5(a) and 5(c), and $k_BT/J = 0.4$ in Figs. 5(b) and 5 (d).

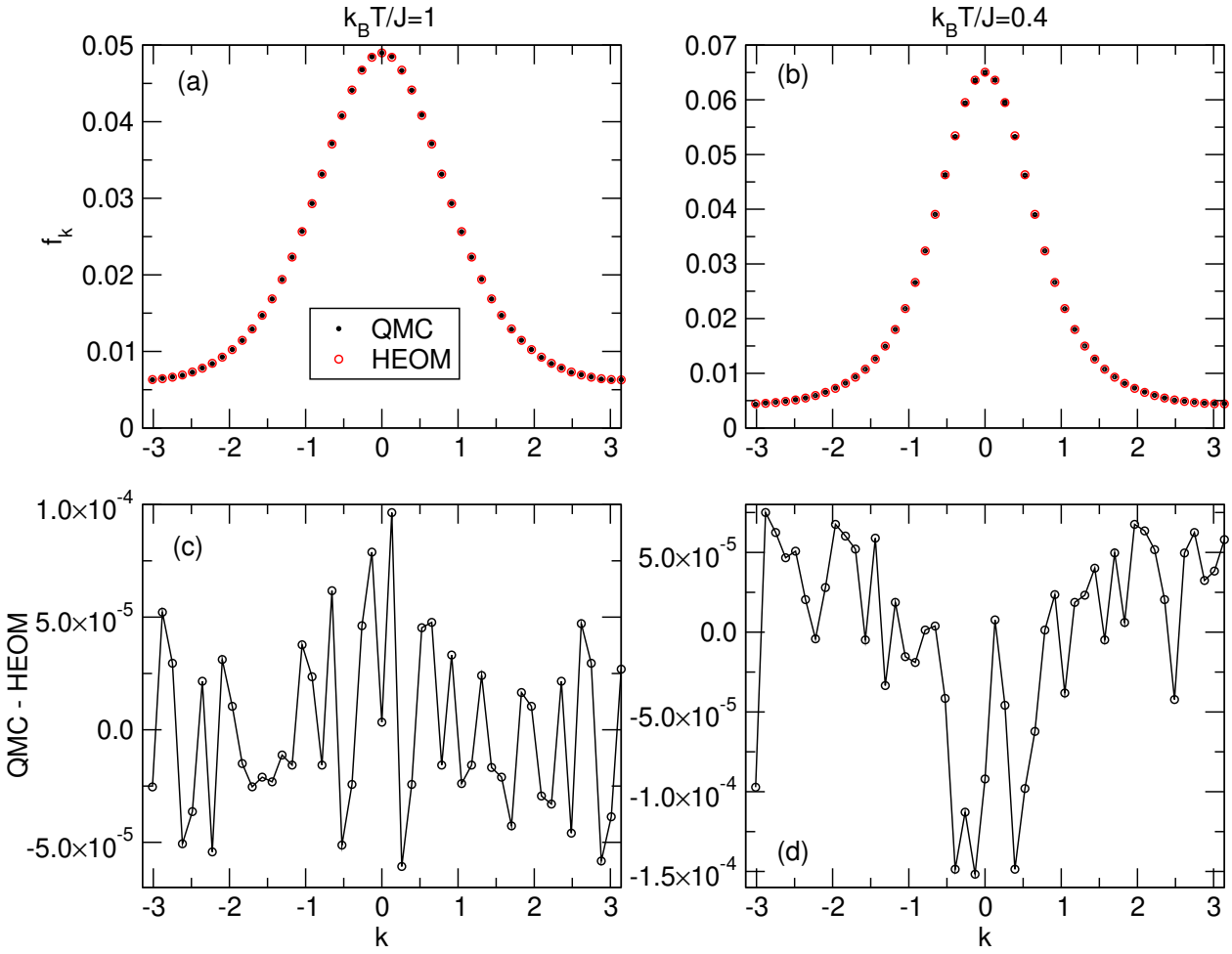

Figure 5. (a) and (b): Electronic momentum distribution f_k computed using QMC (black dots) and HEOM (red empty circles) for (a) $k_BT/J = 1$ and (b) $k_BT/J = 0.4$. QMC error bars are smaller than the size of individual dots. (c) and (d): Difference between QMC and HEOM electronic momentum distributions for (c) $k_BT/J = 1$ and (d) $k_BT/J = 0.4$. The remaining parameters assume the following values: $\hbar\omega_0/J = 1$, $\gamma/J = \sqrt{2}$.

In Fig. 6 we compare QMC and HEOM predictions for the electronic momentum distribution for two different electron–phonon coupling strengths, $\gamma/J = 1$ in Figs. 6(a) and 6(c), and $\gamma/J = 2$ in Figs. 6(b) and 6 (d).

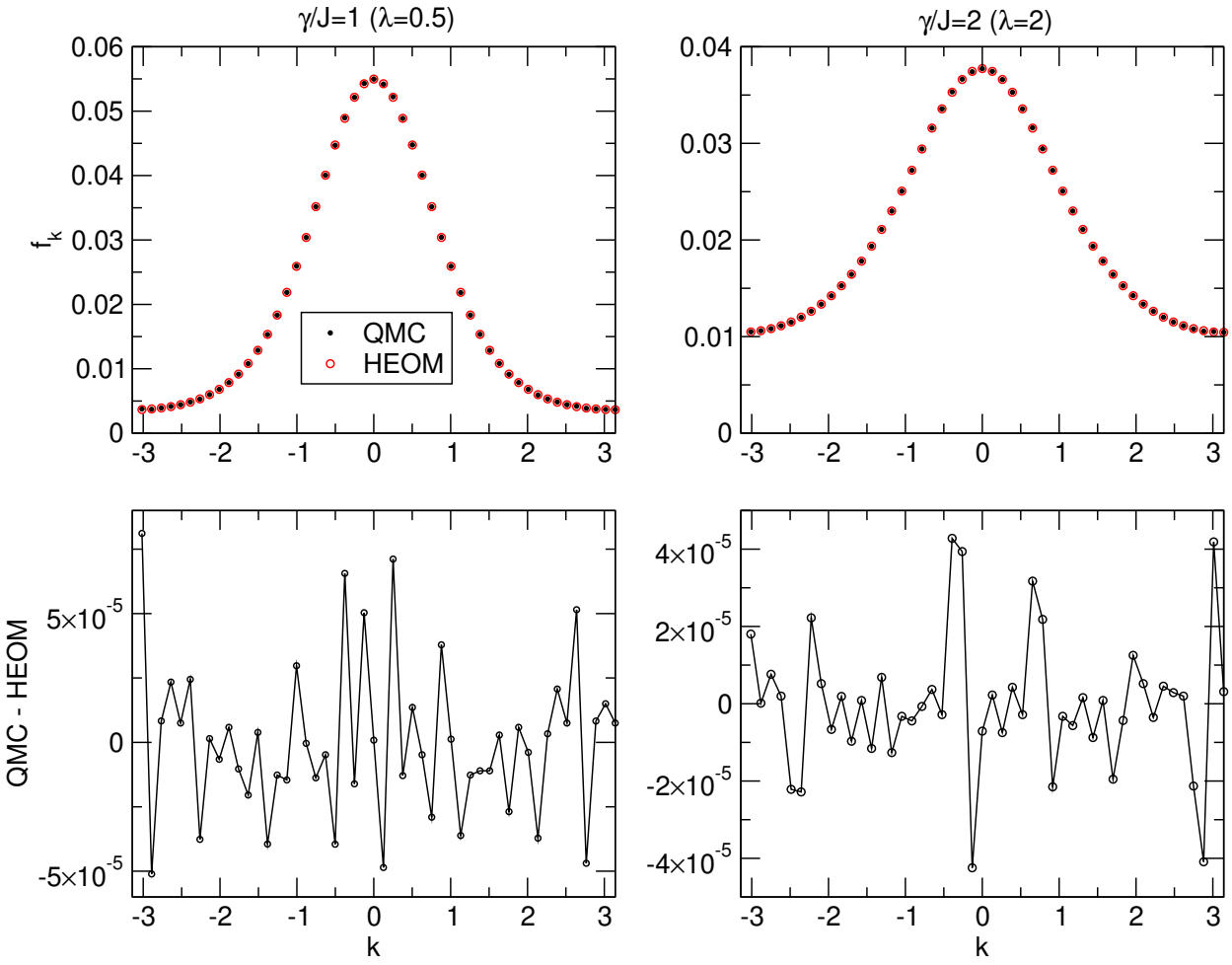

Figure 6. (a) and (b): Electronic momentum distribution f_k computed using QMC (black dots) and HEOM (red empty circles) for (a) $\gamma/J = 1$ and (b) $\gamma/J = 2$. QMC error bars are smaller than the size of individual dots. (c) and (d): Difference between QMC and HEOM electronic momentum distributions for (c) $\gamma/J = 1$ and (d) $\gamma/J = 2$. The remaining parameters assume the following values: $\hbar\omega_0/J = 1$, $k_BT/J = 1$.

VIII. DISCUSSION OF THE HEOM METHOD RESULTS IN THE STRONG-COUPLING ADIABATIC REGIME

Here, we discuss in greater detail the results of the HEOM method in the strong-coupling adiabatic regime, $\hbar\omega_0/J = 0.2$, $\gamma/J = \sqrt{4/5}$, at temperature $k_BT/J = 1$.

We start with Fig. 7, in which we compare the real parts of the envelopes $\mathcal{G}^>(k,t)$ of the greater Green's functions at finite temperature for different maximum depths D of the hierarchy. While the calculations are actually performed up to maximum time $\omega_0 t_{\max} = 400$, which translates to $Jt_{\max}/\hbar = 2000$, Fig. 7 shows only the time window $0 \leq Jt/\hbar \leq 200$. For $Jt/\hbar > 200$, $\mathrm{Re}\,\mathcal{G}^>(k,t)$ exhibits small-amplitude oscillations around 0, the effect that is due to the finite size of the system studied. Although the differences between the results for different D are difficult to appreciate in the real-time domain, they become more visible upon transformation in the real-frequency domain, which is demonstrated in Fig. 8. To obtain $A(k,\omega)$ shown in Fig. 8, we used $G^>(k,t)$ up to the maximum time $Jt_{\max}/\hbar = 2000$ for which we performed the calculations. The positions and intensities of the peaks exhibit appreciable changes with D, which is very different from the situation presented in Fig. 4, where the positions of the peaks do not change with D, while the changes in their intensities are minor. The results presented in Figs. 7 and 8 suggest that the HEOM method experiences problems in the adiabatic regime.

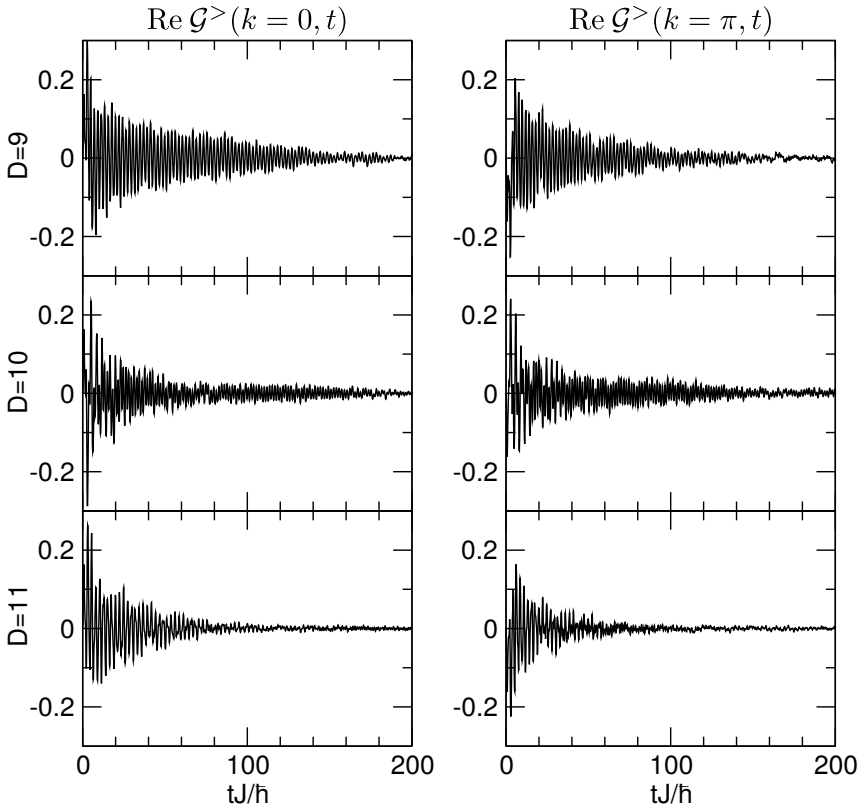

Figure 7. Time dependence of the real part of the envelope of the greater Green's function, $\mathrm{Re}\,\mathcal{G}^>(k,t)$, for three different values of the maximum hierarchy depth ($D = 9$ in the upper panels, $D = 10$ in the middle panels, and $D = 11$ in the lower panels) and for two different values of the dimensionless wave number ($k = 0$ in the left column and $k = \pi$ in the right column). The vertical-axes ranges on all six panels are the same, $[-0.3, 0.3]$. The model parameters assume the following values: $k_BT/J = 1$, $\hbar\omega_0/J = 0.2$, $\gamma/J = \sqrt{4/5}$, $N = 6$.

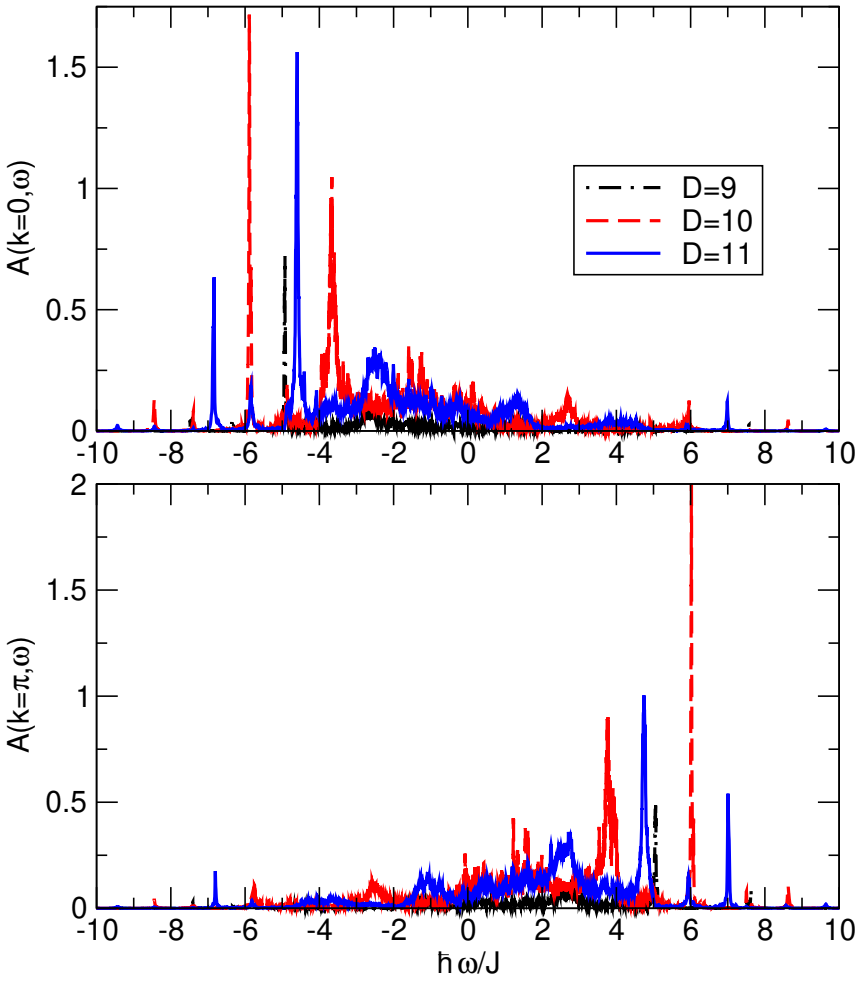

Figure 8. Spectral function $A(k,\omega)$ for three different values of the maximum hierarchy depth ($D = 9$ is represented by dash-dotted black lines, $D = 10$ is represented by dashed red lines, $D = 11$ is represented by solid blue lines) and for two different values of the dimensionless wave number ($k = 0$ in the upper panel and $k = \pi$ in the lower panel). The model parameters assume the following values: $k_BT/J = 1$, $\hbar\omega_0/J = 0.2$, $\gamma/J = \sqrt{4/5}$, $N = 6$.

In order to understand whether the HEOM-method results in the adiabatic limit are reasonable, in Figs. 9(a) and 9(b) we compare the imaginary-time correlation function $C(k,\tau)$ evaluated using the QMC method on a $N = 6$-site chain and the HEOM method on a $N = 6$-site chain with maximum depths $D = 9, 10$, and 11. The results show that, as D is increased, the ratio $\mathrm{QMC}_6/\mathrm{HEOM}_{(6,D)}$ of the QMC and HEOM results (labels are precisely defined in the caption of Fig. 9) becomes closer to unity on the whole imaginary-time interval $0 \leq J\tau/\hbar \leq \beta J$. This suggests that the HEOM results for $D = 11$ are reasonable in the parameter regime studied. These results are shown in Figs. 9(a1) and 9(a2) of the main body of the paper.

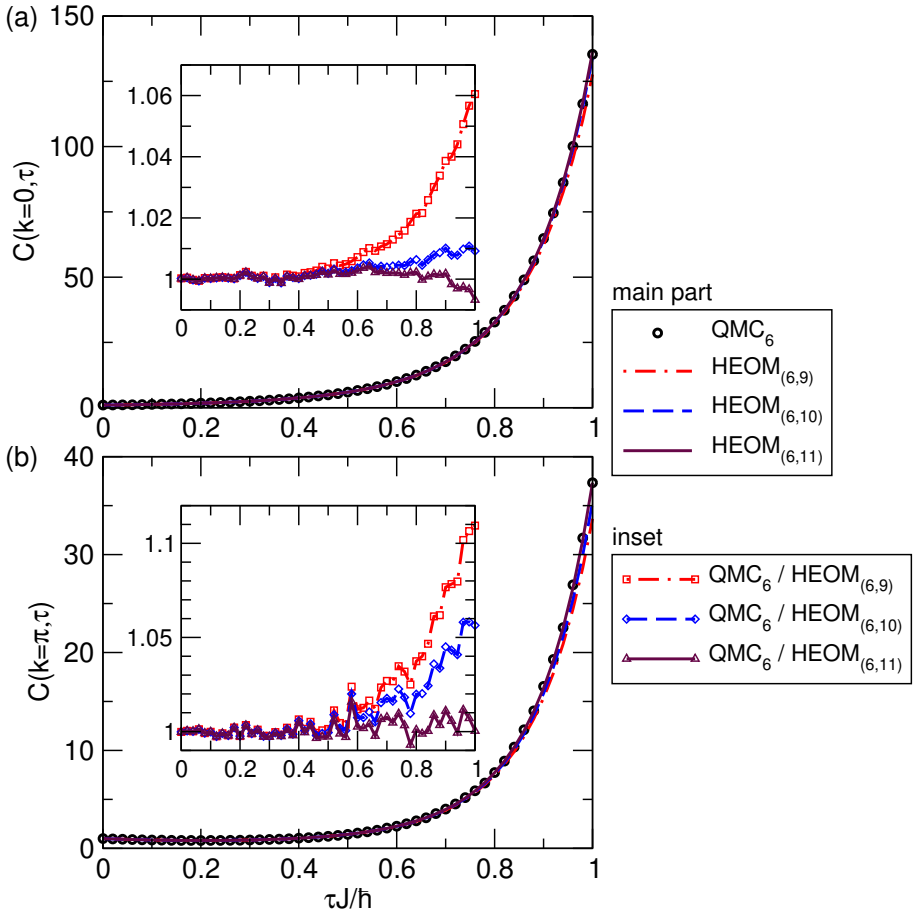

Figure 9. Imaginary-time correlation function $C(k,\tau)$ (a) in the zone center $k=0$ and (b) at the zone edge $k=\pi$ computed using QMC on a 6-site chain (label QMC_6) and HEOM on a 6-site chain with different maximum depths D (label $\mathrm{HEOM}_{(6,D)}$). Insets present the ratio $\mathrm{QMC}_6/\mathrm{HEOM}_{(6,D)}$ for different D. The model parameters assume the following values: $k_BT/J=1$, $\hbar\omega_0/J=0.2$, and $\gamma/J=\sqrt{4/5}$.

IX. INFLUENCE OF THE STATISTICAL SAMPLE SIZE ON QMC RESULTS IN THE INTERMEDIATE-COUPLING LOW-TEMPERATURE REGIME

Here, we present the results for the QMC imaginary-time correlation function $C(k,\tau)$ obtained with different sizes of the statistical sample and compare them to the HEOM results for the same quantity. The calculations are performed on an $N = 8$-site chain (the HEOM method is applied to the chain of the same length) with the following values of model parameters: $\hbar\omega_0/J = 1$, $k_BT/J = 0.4$, and $\gamma/J = \sqrt{2}$. In Figs. 10(a) and 10(b) we show HEOM and QMC data for $C(k = 0,\tau)$ [Fig. 10(a)] and $C(k = \pi,\tau)$ [Fig. 10(b)], while in Figs. 10(c) and 10(d) we compare the ratios $C_{\rm QMC}(k,\tau)/C_{\rm HEOM}(k,\tau)$ for different sizes of the QMC sample.

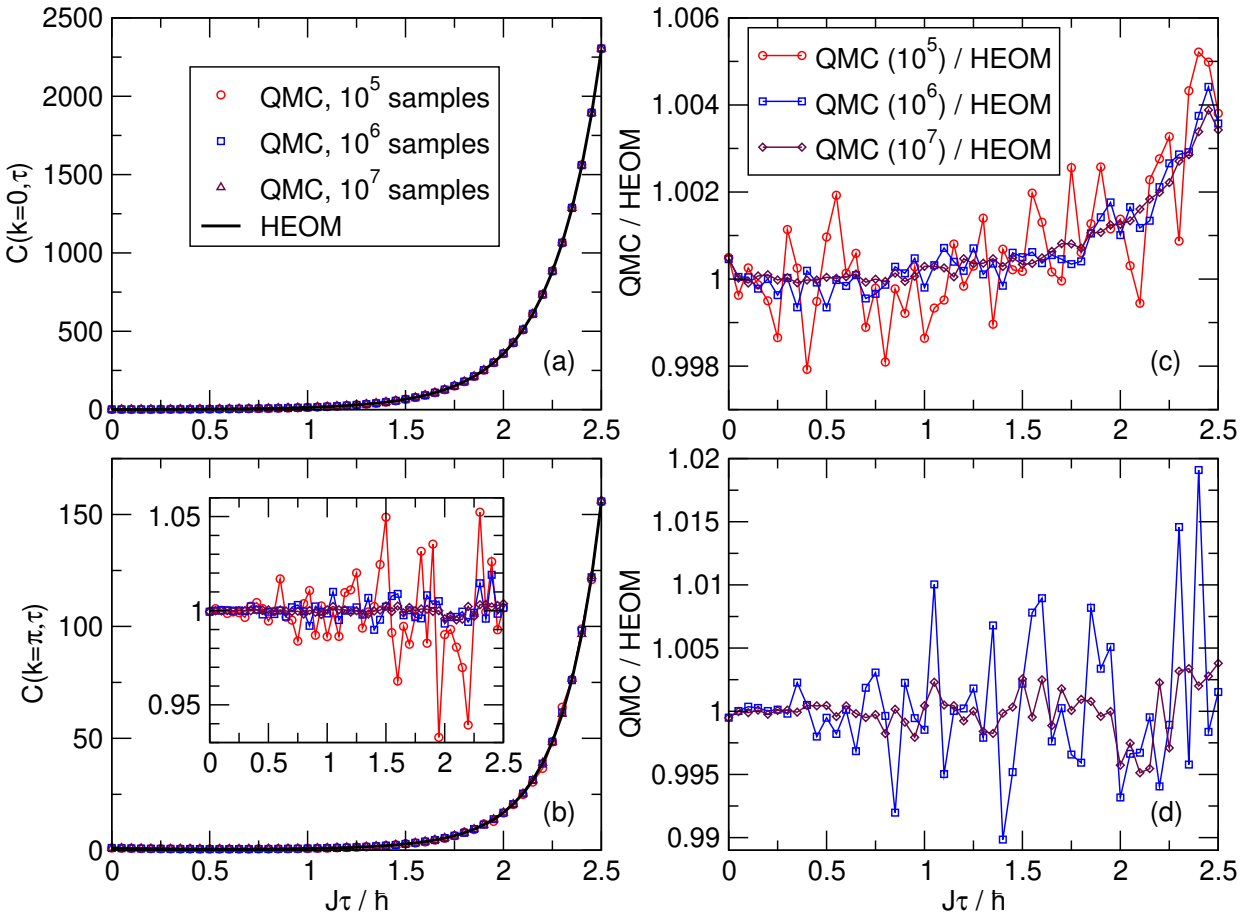

Figure 10. (a) and (b) Imaginary-time correlation function $C(k,\tau)$ in the zone center [(a)] and at the zone edge [(b)] computed using QMC with different statistical sample sizes (empty symbols) and HEOM (solid line). (c) and (d) Ratio of the QMC and HEOM results for different QMC statistical sample sizes. For the sake of clearer visibility, in (d) we show QMC/HEOM only for sample sizes 10^6 and 10^7, while the inset in (b) shows the ratio of the QMC and HEOM results for all sample sizes considered. The model parameters assume the following values: $k_BT/J = 0.4$, $\hbar\omega_0/J = 1$, $\gamma/J = \sqrt{2}$, $N = 8$.

The results presented in Figs. 10(a)–10(d) unambiguously show the reduction in the QMC statistical noise when the sample size is increased from 10^5 to 10^6 and 10^7. While in the zone center decent results are obtained already with 10^5 samples, at the zone edge we need as many as 10^7 samples to reduce the level of the statistical noise.

X. IMAGINARY-TIME CORRELATION FUNCTION IN THE ADIABATIC AND ANTIADIABATIC REGIME

In Figs. 11(a) and 11(b) we present comparison between imaginary-time correlation functions in the zone center [Fig. 11(a)] and at the zone edge [Fig. 11(b)] obtained using the QMC and HEOM methods in the adiabatic regime, $k_BT/J = 1$, $\hbar\omega_0/J = 0.2$, $\gamma/J = \sqrt{4/5}$. The HEOM-method calculation is performed on a $N = 6$-site chain.

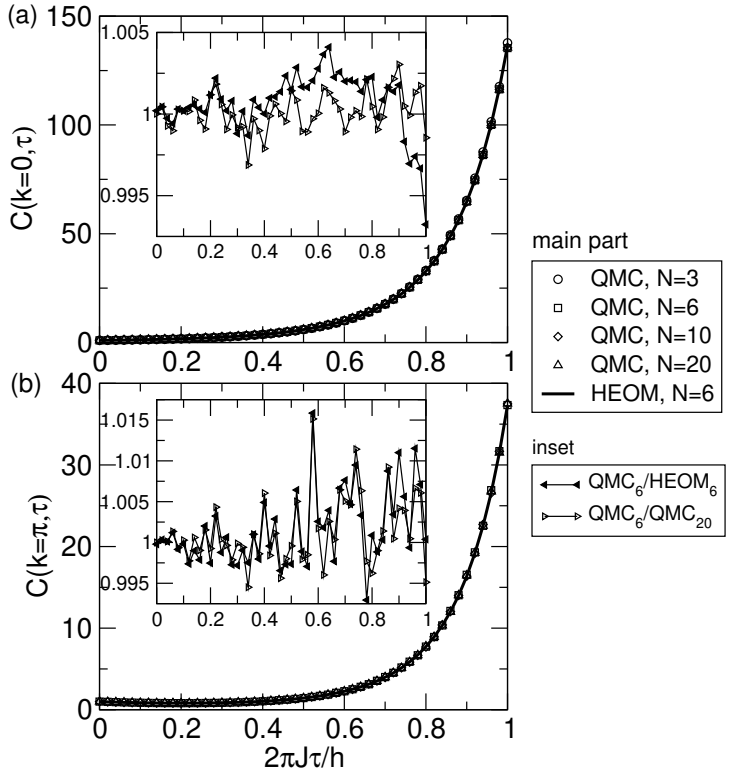

Figure 11. Imaginary time correlation function $C(k, \tau)$ (a) in the zone center $k = 0$ and (b) at the zone edge $k = \pi$ computed using QMC with different chain lengths (empty symbols) and HEOM (solid line). Insets present the ratio of QMC and HEOM results for $N = 6$ (full left-triangles) and the ratio of QMC results for $N = 6$ and $N = 20$ (empty right-triangles). The model parameters assume the following values: $k_BT/J = 1$, $\hbar\omega_0/J = 0.2$, $\gamma/J = \sqrt{4/5}$.

In Figs. 12(a) and 12(b) we present comparison between imaginary-time correlation functions in the zone center [Fig. 12(a)] and at the zone edge [Fig. 12(b)] obtained using the QMC and HEOM methods in the antiadiabatic regime, $k_BT/J = 1$, $\hbar\omega_0/J = 3$, $\gamma/J = \sqrt{12}$. The HEOM-method calculation is performed on a $N = 6$-site chain.

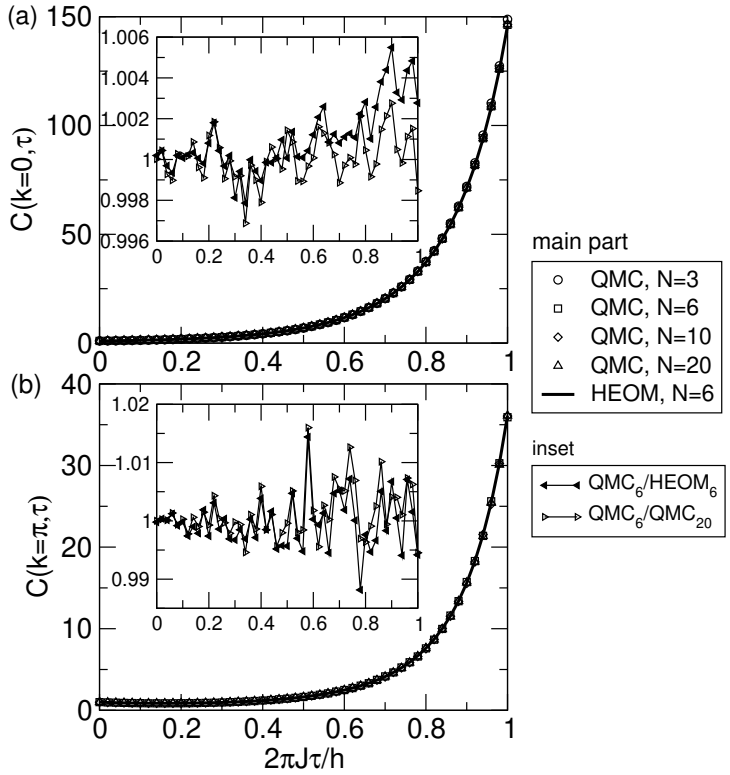

Figure 12. Imaginary time correlation function $C(k, \tau)$ (a) in the zone center $k = 0$ and (b) at the zone edge $k = \pi$ computed using QMC with different chain lengths (empty symbols) and HEOM (solid line). Insets present the ratio of QMC and HEOM results for $N = 6$ (full left-triangles) and the ratio of QMC results for $N = 6$ and $N = 20$ (empty right-triangles). The model parameters assume the following values: $k_BT/J = 1$, $\hbar\omega_0/J = 3$, $\gamma/J = \sqrt{12}$.

* veljko.jankovic@ipb.ac.rs
† nenad.vukmirovic@ipb.ac.rs

[1] G. Mahan, *Many-Particle Physics* (Kluwer Academic, New York, 2000).
[2] I. S. Gradshteyn and I. M. Ryzhik, *Table of Integrals, Series, and Products* (Elsevier Academic Press, 2007).
[3] H. Liu, L. Zhu, S. Bai, and Q. Shi, "Reduced quantum dynamics with arbitrary bath spectral densities: Hierarchical equations of motion based on several different bath decomposition schemes," J. Chem. Phys. **140**, 134106 (2014).